Singularity Formation in a Cylindrical and a Spherical Vortex Sheet

Monika Nitsche

Department of Mathematics and Statistics, University of New Mexico, Humanities 415,
Albuquerque, New Mexico 87131-1141
E-mail: nitsche@math.unm.edu

The evolutions of the planar and axisymmetric vortex sheets generated by the impulsive motion of a cylinder and a sphere, respectively, are compared numerically. The numerical method addresses difficulties that occur in the axisymmetric case near the axis of symmetry. The planar vortex sheet is known to develop a branch point singularity in finite time. Comparison of the planar and axisymmetric solutions indicates that the axisymmetric sheet develops a branch point singularity as well, and that it is of the same order p as the planar singularity. The value of p is consistent with 3/2. © 2001 Academic Press

Key Words: vortex sheet; singularity formation; axisymmetric vortex sheets.

1. INTRODUCTION

Consider a cylinder immersed in inviscid fluid which is given an impulse in a direction normal to itself. The resulting potential flow is induced by a planar vortex sheet in place of the cylinder. Similarly, the potential flow past an impulsively started sphere is induced by an axisymmetric vortex sheet in place of the sphere. This paper studies the evolution of the planar and axisymmetric vortex sheets under their self-induced velocity, as if the cylinder and sphere were dissolved and the fluid within them allowed to move with the flow. There is no surface tension present.

Planar vortex sheets with analytic initial conditions are known to lose their analyticity in finite time. This was first shown by Moore [20] for a periodical perturbation of a flat vortex sheet. Using approximate evolution equations for the Fourier coefficients, he found that the vortex sheet coordinates, parametrized by the circulation Γ, develop a branch point singularity proportional to $\Gamma^{3/2}$. The singularity formation was confirmed by Meiron, Baker, and Orszag [19] using Taylor series expansions, and by Krasny [17] and Shelley [28] using the point vortex approximation. A 3/2 branch point singularity was also found in planar Boussinesq flow (Pugh [25]), and in Rayleigh Taylor flow (Baker, Caflisch and Siegel [2]).

Recent analytical work suggests that Moore's 3/2 singularity is generic for planar vortex sheets (Caflisch *et al.* [7], Cowley, Baker, and Tanveer [12]).

Much less is known about fully 3D or axisymmetric vortex sheets. Ishihara and Kaneda [15, 16] and Brady and Pullin [6] considered certain 3D perturbations of a flat vortex sheet and found analytical evidence of singularity formation based on Moore's analysis [6, 15], as well as numerical evidence [16]. For axisymmetric vortex sheets, the numerical results of Pugh [25], Nitsche [23], and Nie and Baker [22] indicate the formation of a singularity. Hu [14] recently showed at least formally that 3D and planar vortex sheets share the same type of singularity. The goal of the present paper is to compare planar and axisymmetric singularity formation numerically.

The numerical method used to compute the vortex sheet evolution is based on evaluating the singular integrals that represent the vortex sheet velocity. In the planar case, these integrals are computed accurately with either van de Vooren's [31] approximation or the alternate point vortex approximation (Baker [1], Shelley [28]), as has previously been done by Rottman and Stansby [27]. In the axisymmetric case, a complication occurs that is not present in the planar case. For points near the axis of symmetry, the integrands have large variations which make it difficult to evaluate the velocity accurately (Baker, Meiron, and Orszag [3]). De Bernadinis and Moore [5] computed the axisymmetric velocity using a third order accurate quadrature rule and showed that there is a large loss of accuracy as the axis is approached, even though the vortex sheet is smooth. Nitsche [24] showed that this loss of accuracy occurs for standard quadrature rules of arbitrarily high order. At any given point on the vortex sheet, the discretization error converges at the correct rate, but it does not converge uniformly. The maximum error is always of size $O(h)$, where h is the mesh size. The difficulty is caused by the behaviour of coefficients multiplying the logarithmic terms in the axisymmetric integrands, as well as derivatives at the endpoints. Their values are shown to become unbounded as the axis is approached.

The loss of accuracy makes it difficult to resolve the axisymmetric singularity formation. Pugh [25] reduced the size of the errors near the axis using asymptotic expansions of the integrals, but found that for computationally feasible mesh sizes the error remained too large. Nie and Baker [22] used local mesh refinement to more accurately evaluate the integrals. For each integral, they introduced new mesh points, based on an interpolant of the vortex sheet, and were able to sufficiently reduce the error near the axis.

Here we apply a method proposed by Nitsche [24] to address the difficulty in the axisymmetric case. It is based on an analytical approximation of the integrand whose integral can be accurately precomputed for all times. By subtracting the approximation, a quadrature rule is obtained that converges uniformly over the vortex sheet at no additional cost, and removes the loss of accuracy near the axis. This method has been used by Ceniceros and Si [11] to resolve axisymmetric Darcian flow. Below, we describe a fifth order accurate extension of the method. The axisymmetric simulations are then compared to the planar ones. The main result is evidence that the planar and axisymmetric flows behave almost identically near a critical time, indicating that the axisymmetric sheet develops a branch point singularity as well and that it is of the same type as the planar one.

The paper is organized as follows. Section 2 presents the initial conditions and the governing equations. Section 3 describes the numerical method. It illustrates the differences between the planar and the axisymmetric integrands responsible for the axisymmetric complication and describes the quadrature rules used in each case. Section 4 presents the planar

and axisymmetric simulations and compares the results. The results are summarized in Section 5.

2. PROBLEM FORMULATION

2.1. Initial Conditions

Let (x, y, z) be a Cartesian coordinate system such that the initial cylinder and sphere are centered at the origin and the z-axis is the axis of the cylinder (Fig. 1a, b). The initial radius is a and the initial velocity inside the cylinder/sphere is $(U, 0, 0)$. The initial velocity outside the cylinder/sphere is determined by the stream function in the upper $x–y$ plane,

$$\psi_{2d}(r, \theta) = \frac{a^2 U}{r} \sin \theta, \quad \psi_{3d}(r, \theta) = \frac{a^3 U}{2r} \sin^2 \theta, \quad 0 \le \theta \le \pi, \quad r \ge a \qquad (2.1)$$

(Batchelor [4], Sections 6.6, 6.8). Here r, θ are polar coordinates, and the subscripts $2d$ and $3d$ refer to the planar and axisymmetric case respectively.

The evolving vortex sheets are described by their cross section with the upper $x–y$ plane and by the circulation distribution. The cross section (Fig. 1c) is a curve $(x(\alpha, t), y(\alpha, t))$ parametrized by a Lagrangian parameter α. The circulation $\Gamma(\alpha)$ is given by $d\Gamma/ds = \sigma(s, t)$, where s is arclength, and σ is the vortex sheet strength, that is, the jump in the tangential velocity across the sheet. From (2.1) it follows that the initial velocity jump is

$$\sigma_{2d}(s, 0) = 2U \sin \theta, \quad \sigma_{3d}(s, 0) = \frac{3}{2} U \sin \theta, \quad s = a\theta. \qquad (2.2)$$

We choose α to equal the angle θ at time zero and $\Gamma(\alpha)$ to be the total circulation between $(x(\alpha, t), y(\alpha, t))$ and the foremost point on the sheet, $\Gamma(\alpha) = \int_0^{s(\alpha)} \sigma(s, 0) \, ds$. The total circulation in the upper $x–y$ plane, $\Gamma_T = \Gamma(\pi)$, is

$$\Gamma_{T,2d} = 4Ua, \quad \Gamma_{T,3d} = 3Ua. \qquad (2.3)$$

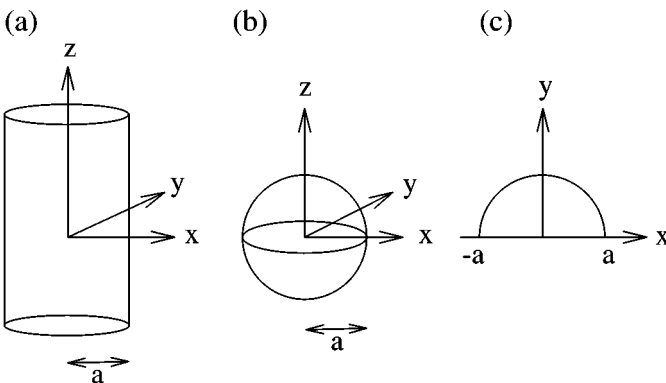The flow is nondimensionalized with respect to the initial radius a and the total circulation

FIG. 1. Sketch illustrating the coordinate system and initial vortex sheets (a, b) and their cross section with the upper $x–y$ plane (c).

Γ_T. With this choice, the initial vortex sheet is given by

$$x(\alpha, 0) = \cos\alpha, \quad y(\alpha, 0) = \sin\alpha, \quad \Gamma(\alpha) = (1 - \cos\alpha)/2, \quad 0 \le \alpha \le \pi. \quad (2.4)$$

The corresponding nondimensional initial velocity is $U_{2d} = 1/4$ and $U_{3d} = 1/3$.

2.2. Evolution Equation

The vortex sheets $(x(\alpha, t), y(\alpha, t))$ with circulation $\Gamma(\alpha)$ are a superposition of vortex elements with strength $d\Gamma = \Gamma'(\alpha)\,d\alpha$. These elements are counterrotating pairs of vortex lines in the planar case, and circular vortex filaments in the axisymmetric case. The stream function at (x, y) induced by an element at $(\tilde{x}, \tilde{y})$ of unit strength is

$$\psi_{2d}(x, y, \tilde{x}, \tilde{y}) = -\frac{1}{4\pi} \log \frac{(x - \tilde{x})^2 + (y - \tilde{y})^2}{(x - \tilde{x})^2 + (y + \tilde{y})^2}, \quad (2.5a)$$

$$\psi_{3d}(x, y, \tilde{x}, \tilde{y}) = \frac{y\tilde{y}}{4\pi} \int_0^{2\pi} \frac{\cos\theta\,d\theta}{((x - \tilde{x})^2 + y^2 + \tilde{y}^2 - 2y\tilde{y}\,\cos\theta)^{1/2}}. \quad (2.5b)$$

The corresponding velocity at (x, y) induced by an element at $(\tilde{x}, \tilde{y})$ is

$$(u_{2d}, v_{2d}) = \left(\frac{\partial\psi_{2d}}{\partial y}, -\frac{\partial\psi_{2d}}{\partial x}\right), \quad (u_{3d}, v_{3d}) = \left(\frac{1}{y}\frac{\partial\psi_{3d}}{\partial y}, -\frac{1}{y}\frac{\partial\psi_{3d}}{\partial x}\right), \quad (2.6)$$

and the total velocity induced by the vortex sheets is obtained by superposition,

$$(u, v)(x, y) = \int_0^{\pi} (u, v)(x, y, x(\alpha, t), y(\alpha, t))\Gamma'(\alpha)\,d\alpha. \quad (2.7)$$

For points (x, y) on the vortex sheets, the integrals in (2.7) are singular and are evaluated in the principal value sense, which effectively assigns to the sheets the average of the velocities on either side of them. The sheets evolve under self-induction,

$$\frac{dx}{dt}(\alpha, t) = u(x(\alpha, t), y(\alpha, t)), \quad \frac{dy}{dt}(\alpha, t) = v(x(\alpha, t), y(\alpha, t)), \quad (2.8)$$

with the given initial conditions (2.4).

3. NUMERICAL METHOD

The vortex sheets are discretized by $N + 1$ vortex elements at $(x_j, y_j) = (x(\alpha_j, t), y(\alpha_j, t))$, $j = 0, \ldots, N$, corresponding to a uniform mesh in α, $\alpha_j = jh$, $h = \pi/N$. The velocity of the jth element is

$$\frac{dx_j}{dt} = \int_0^{\pi} G^u(\alpha, \alpha_j, t)\,d\alpha, \quad \frac{dy_j}{dt} = \int_0^{\pi} G^v(\alpha, \alpha_j, t)\,d\alpha, \quad (3.1)$$

where G^u, G^v are the integrands in (2.7) evaluated at $(x, y) = (x_j, y_j)$ (see [24] for the axisymmetric case). The numerical method consists of approximating the integrals of G^u, G^v

in (3.1) by a quadrature rule, integrating the resulting system of ordinary differential equations by the fourth order Runge–Kutta scheme, and applying a Fourier filter. The main portion of this section discusses the quadrature rules to be used. It illustrates the difference between the planar and the axisymmetric case, and describes the remedy for the difficulty occuring in the axisymmetric one.

3.1. Planar vs Axisymmetric Case

The planar and axisymmetric integrands G have expansions in $\alpha - \alpha_j$ of the form

$$G_{2d}(\alpha, \alpha_j, t) = \tilde{G}_{2d}(\alpha, \alpha_j, t) + \frac{c_{-1,2d}(\alpha_j, t)}{\alpha - \alpha_j},$$

$$G_{3d}(\alpha, \alpha_j, t) = \tilde{G}_{3d}(\alpha, \alpha_j, t) + \frac{c_{-1,3d}(\alpha_j, t)}{\alpha - \alpha_j}$$

$$+ \sum_{k=0}^{\infty} c_{k,3d}(\alpha_j, t)(\alpha - \alpha_j)^k \log |\alpha - \alpha_j|. \tag{3.2}$$

Here $\tilde{G}$ is smooth as long as the vortex sheet is smooth. Sidi and Israeli [29] derive quadrature rules based on a uniform mesh that integrate singular functions of the form (3.2) to arbitrary accuracy. In the planar case, their simplest quadrature rule turns out to be exponentially accurate, and equals the one used by van de Vooren [31]. In the axisymmetric case, we will see that all of their quadrature rules lose accuracy when α_j is near the axis and have maximum errors of size $O(h)$, making it difficult to resolve the axisymmetric vortex sheet motion. As explained below, the reason for the complication in the axisymmetric case is not the presence of the additional logarithmic terms given in (3.2), but the behaviour of the coefficients c_k and of derivatives of G on the axis, as a function of α_j.

The quadrature rules given by Sidi and Israeli [29] for integrals of the form (3.1), (3.2) are

$$\fint_0^\pi G(\alpha, \alpha_j, t)\, d\alpha \approx Q[G]_{[0,\pi]}^h, \tag{3.3}$$

where

$$Q[G]_{[0,\pi]}^h = h \sum_{k \neq j}{}' G(\alpha_k, \alpha_j, t) + h\tilde{G}(\alpha_j, \alpha_j, t) + c_0(\alpha_j, t)h \log \frac{h}{2\pi}$$

$$+ \sum_{\substack{k=2 \\ k\ \text{even}}}^{2m} \nu_k c_k(\alpha_j, t)h^{k+1} + \sum_{\substack{k=1 \\ k\ \text{odd}}}^{2m+1} \gamma_k \left[G^{(k)}(\pi, \alpha_j, t) - G^{(k)}(0, \alpha_j, t) \right] h^{k+1}. \tag{3.4}$$

Here $m \geq 0$, with larger values of m corresponding to higher order approximations. For $m = 0$, it is implied that the fourth term in (3.4) is absent. The prime on the summation indicates that the first and last summands are weighted by $1/2$. The derivatives $G^{(k)}$ are taken with respect to the variable of integration α, and the constants ν_k, γ_k are defined in terms of the Riemann zeta function. The first term in (3.4) is the trapezoid rule approximation of a principal value integral, as used in the point vortex approximation. The second term

is the correction given by van de Vooren [31]. The third and fourth terms account for the logarithmic terms in (3.2). The last term corresponds to the Euler–MacLaurin series for the error in the trapezoid rule [13], Section 7.4). The approximation error is

$$E[G]^h_{[0,\pi]}(\alpha_j, t) = \int_0^\pi G(\alpha, \alpha_j, t)\, d\alpha - Q[G]^h_{[0,\pi]} = \sum_{\substack{k=2m+2 \\ k\ even}}^{2n+2} v_k c_k(\alpha_j, t) h^{k+1}$$

$$+ \sum_{\substack{k=2m+3 \\ k\ odd}}^{2n+3} \gamma_k \big[G^{(k)}(\pi, \alpha_j, t) - G^{(k)}(0, \alpha_j, t) \big] h^{k+1} + O(h^{2n+5}) \qquad (3.5)$$

for any integer $n \geq m$.

Consider the quadrature rule (3.4) with $m = 0$ and the associated approximation error (3.5). In the planar case, the logarithmic terms are absent, so $c_{k,2d} = 0$ for $k \geq 0$. One can also show that the planar integrands G_{2d} have a smooth extension across the axis that is even, so that all odd derivatives $G^{(k)}_{2d}$ vanish at the endpoints, $\alpha = 0, \pi$. Thus, (3.5) shows that in the planar case, the quadrature rule with $m = 0$ is exponentially accurate. This is the approximation used by van de Vooren [31]. The alternate point vortex approximation introduced by Baker [1] and used by Shelley [28] is another exponentially accurate approximation which is more efficient and eliminates the need to compute the value of $\tilde{G}(\alpha_j, \alpha_j, t)$. For this paper we computed the planar flow using both of these methods and found that the results from the two methods are indistinguishable.

Now consider the quadrature rule with $m = 0$ in the axisymmetric case. The axisymmetric integrand G_{3d} contains the logarithmic terms, $c_{k,3d} \neq 0$ for all $k \geq 0$. Furthermore, one can show that G_{3d} has a smooth extension across the axis that is odd instead of even, and that all odd derivatives $G^{(k)}_{3d}$ except for the first one are nonzero at the endpoints, $\alpha = 0, \pi$. Thus, (3.5) shows that in the axisymmetric case, the quadrature rule with $m = 0$ is $O(h^3)$. This is the quadrature rule derived by de Bernadinis and Moore [5].

De Bernadinis and Moore [5], however, observed that their quadrature rule loses much accuracy near the axis. It turns out that while the approximation error (3.5) converges at the correct rate pointwise, it does not converge uniformly in α_j, and that the maximum error is $O(h)$ instead of $O(h^3)$. Nitsche [24] showed that the problem arises because the coefficients $c_{k,3d}$ and $G^{(k)}_{3d}$ become unbounded as $\alpha_j \to 0$,

$$c^u_{k,3d}(\alpha_j, t) \sim \frac{1}{\alpha_j^k}, \quad c^v_{k,3d}(\alpha_j, t) \sim \frac{1}{\alpha_j^{k-1}}, \qquad (3.6a)$$

$$G^{(k),u}_{3d}(0, \alpha_j, t) \sim \frac{1}{\alpha_j^k}, \quad G^{(k),v}_{3d}(0, \alpha_j, t) \sim \frac{1}{\alpha_j^{k-1}}. \qquad (3.6b)$$

Similar behaviour occurs as $\alpha_j \to \pi$. For a fixed mesh, (3.6) shows that the values of $c_{k,3d}$ and $G^{(k)}_{3d}$ are largest when $j = 1$, or $\alpha_j = \alpha_1 = h$, and

$$c^u_{k,3d}(\alpha_1, t) \sim \frac{1}{h^k}, \quad c^v_{k,3d}(\alpha_1, t) \sim \frac{1}{h^{k-1}}, \qquad (3.7a)$$

$$G^{(k),u}_{3d}(0, \alpha_1, t) \sim \frac{1}{h^k}, \quad G^{(k),v}_{3d}(0, \alpha_1, t) \sim \frac{1}{h^{k-1}}. \qquad (3.7b)$$

Substituting (3.7) into (3.5) thus shows that the maximum errors in the integration of G_{3d}^u and G_{3d}^v occur when $j = 1$ and are of size $O(h)$ and $O(h^2)$, respectively. This is true for any value of m. That is, no matter how accurate a quadrature rule (3.4) is used, the maximum errors converge to first and second order only.

In summary, the fact that unlike the planar integrand, the axisymmetric one contains logarithmic terms and is odd across the axis and not even, accounts for the fact that the axisymmetric quadrature is $O(h^{2m+3})$ and not exponentially accurate as the planar one. This does not present a problem, since m can be chosen to be as large as desired. The complication in the axisymmetric case is due to the unboundedness given by (3.6), which accounts for the fact that the maximum error is of size $O(h)$, independently of m.

3.2. Corrected Axisymmetric Quadrature Rule

Figure 2(a, b) illustrates the loss of accuracy of the axisymmetric quadrature rule (3.4) with $m = 1$, which is $O(h^5)$. (Here, we need the values $\gamma_1 = -1/12$, $\gamma_3 = 1/720$, and $\nu_2 = -0.06089691411678654156$.) The figure plots the discretization error (e_u, e_v) in the initial axisymmetric velocity $\oint G_{3d}^u(\alpha, \alpha_j, 0)\, d\alpha$, $\oint G_{3d}^v(\alpha, \alpha_j, 0)\, d\alpha$, computed with $h = \pi/N$ and $N = 50, 100, 200, 400, 800$. The figure shows that for fixed α_j the error converges at the correct rate, but that the approximation loses accuracy near the axis. As discussed, the maximum errors occur at one gridpoint from the axis and decay as $O(h)$ in Fig. 2(a), and as $O(h^2)$ in Fig. 2(b). Note that the large loss of accuracy near the axis occurs even though the vortex sheet is perfectly smooth there.

Figure 2(c) plots the magnitude of the Fourier coefficients $\hat{e}_k$ of the complex error $e_u + i e_v$. Because of the large values of e_u, e_v near the axis, the discretization error contains high wavenumber modes of large amplitude. An analysis of the data indicates that the modes $\hat{e}_{\pm N}$ decay as $O(h^2)$. In time, these high wavenumber modes grow due to the Kelvin–Helmholtz instability of the vortex sheet. A Fourier filter (Krasny [17]), originally used to control the growth of roundoff error, can be used to control the growth of the discretization error. However, the level at which such a filter would have to be applied introduces global $O(h^2)$ errors, which makes it prohibitively expensive to resolve the axisymmetric singularity formation.

It is therefore not practical to use the quadrature rule (3.4) for the axisymmetric case. Nie and Baker [22] addressed the problem using local mesh refinement to more accurately compute the integrals describing the vortex sheet velocity. At each timestep, they use an interpolant of the vortex sheet to introduce as many new quadrature points as needed so that the discretization error is uniformly small. They also use a quadrature rule that integrates logarithmic terms accurately, thereby minimizing the required number of inserted points. The resulting approximation is as accurate as the interpolant, and the discretization error is smooth.

Here, we take the approach developed by Nitsche [24], based on an analytical approximation B of the integrand G near the axis. The approximation is chosen such that

(i) B has a self-similar form that is essentially time independent, and
(ii) $G - B$ does not have the problematic property (3.6) of G.

As a result of (i), the integral of B can be accurately precomputed. As a result of (ii), the integration of $G - B$ does not lose accuracy near the axis. The method consists of precomputing the integral of B and integrating $G - B$ instead of G at each timestep, at no
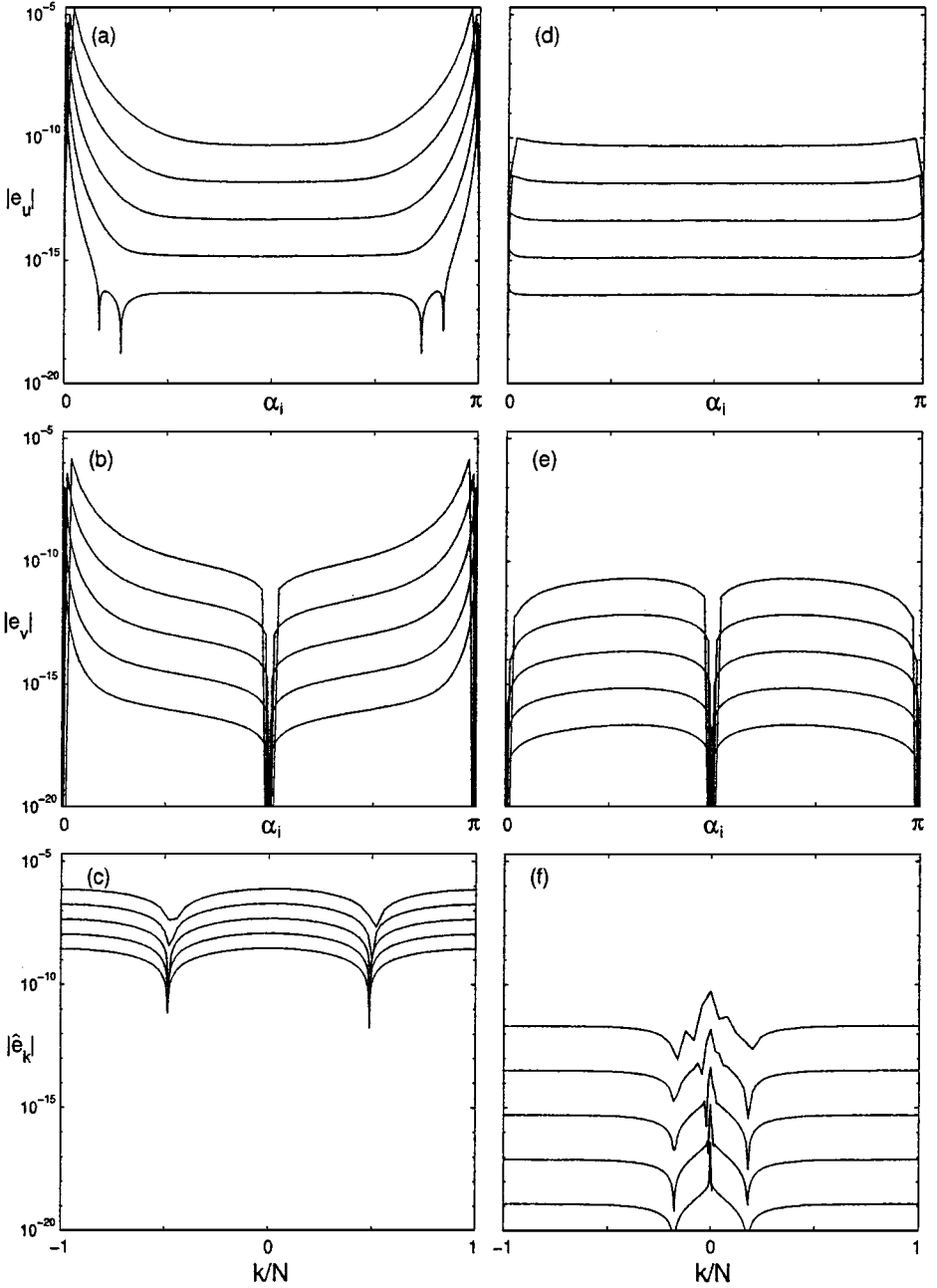
FIG. 2. Discretization error in the initial axisymmetric velocity at (x_j, y_j), $j = 0, \ldots, N$, computed with $N = 50, 100, 200, 400, 800$. The left column shows the results using the $O(h^5)$ quadrature (3.4) with $m = 1$. The right column shows the results using the corrected quadrature (3.12). (a,d) Absolute error $|e_u|$ vs. α_j, (b,e) absolute error $|e_v|$ vs. α_j, (c,f) Fourier coefficients $|\hat{e}_k|$ of the complex error $e_u + i e_v$ vs. k.

additional computational cost. In this paper we use an $O(h^5)$ version of the method, which is an extension of the version presented in [24]. The description below is meant to summarize the basic ideas and present a slightly simpler implementation than the one given in [24].

The method requires approximations B^{le} and B^{ri} of G near the left and right endpoints, $\alpha, \alpha_j \approx 0$ and $\alpha, \alpha_j \approx \pi$. One can show that for $\alpha, \alpha_j \approx 0$,

$$G^u(\alpha, \alpha_j, t) \approx B^{u,le}(\alpha, \alpha_j, t) = b_0^u(t) B_0^u \left(\frac{\alpha}{\alpha_j} \right) + \alpha_j^2 \sum_{k=1}^{3} b_k^u(t) B_k^u \left(\frac{\alpha}{\alpha_j} \right) + O(\alpha^4, \alpha_j^4),$$

$$G^v(\alpha, \alpha_j, t) \approx B^{v,le}(\alpha, \alpha_j, t) = \alpha_j b_0^v(t) B_0^v \left(\frac{\alpha}{\alpha_j} \right) + \alpha_j^3 \sum_{k=1}^{4} b_k^v(t) B_k^v \left(\frac{\alpha}{\alpha_j} \right) + O(\alpha^5, \alpha_j^5),$$

$$(3.8)$$

with coefficients $b_k^{u,v}$ and functions $B_k^{u,v}$ as given in [24]. Note that since the functions $B_k^{u,v}$ are time independent, their integrals can be precomputed to desired accuracy. Thus we numerically integrate $G - B^{le}$ instead of G, over some domain containing the lower bound $\alpha = 0$. It will be convenient to choose different upper bounds for the integration of G and of B^{le}. We approximate

$$\fint_0^\pi G \, d\alpha = \fint_0^\pi G \, d\alpha - \fint_0^{\alpha_j L} B^{le} \, d\alpha + \fint_0^{\alpha_j L} B^{le} \, d\alpha \approx Q[G]_{[0,\pi]}^h - Q[B^{le}]_{[0,\alpha_j L]}^h + \fint_0^{\alpha_j L} B^{le} \, d\alpha$$

$$= Q[G]_{[0,\pi]}^h + E_Q[B^{le}]_{[0,\alpha_j L]}^h, \tag{3.9}$$

where Q is the fifth order approximation (3.4) with $m = 1$. The error $E_Q[B^{le}]_{[0,\alpha_j L]}^h$ is a correction to the quadrature rule Q. Here, L has to be large enough so that $[0, \alpha_j L]$ includes the interval where B approximates G well; we choose $L = 100$. The upper bound $\alpha_j L$ is chosen so that the correction can be precomputed conveniently. By substituting (3.8) into

$$E_Q[B^{le}]_{[0,\alpha_j L]}^h = \fint_0^{\alpha_j L} B^{le}(\alpha, \alpha_j, t) \, d\alpha - Q[B^{le}]_{[0,\alpha_j L]}^h \tag{3.10}$$

and making the change of variables $\eta = \alpha/\alpha_j$, $\Delta \eta = \Delta\alpha/\alpha_j = 1/j$, the correction $E_Q[B^{le}]$ can be rewritten as

$$E_Q[B^{u,le}]_{[0,\alpha_j L]}^h = \alpha_j b_0^u(t) E_Q \left[B_0^u \right]_{[0,L]}^{1/j} + \alpha_j^3 \sum_{k=1}^{3} b_k^u(t) E_Q \left[B_k^u \right]_{[0,L]}^{1/j} \tag{3.11a}$$

$$E_Q[B^{v,le}]_{[0,\alpha_j L]}^h = \alpha_j^2 b_0^v(t) E_Q \left[B_0^v \right]_{[0,L]}^{1/j} + \alpha_j^4 \sum_{k=1}^{4} b_k^v(t) E_Q \left[B_k^v \right]_{[0,L]}^{1/j}. \tag{3.11b}$$

In this form, the numbers $E_Q[B_k]_{[0,L]}^{1/j}$ are independent of h as well as t and can be conveniently precomputed for all mesh sizes to desired accuracy. Only the coefficients b_k, which depend on derivatives of $x(\alpha, t)$, $y(\alpha, t)$, and $\Gamma(\alpha)$ at the endpoint $\alpha = 0$, have to be computed at each timestep. Equation (3.11) also shows that the maximum corrections occur when $j = 1$ and are of size $O(h)$ and $O(h^2)$, respectively.

The corrections $E_Q[B^{le}]^h_{[0,\alpha_j L]}$ in (3.9) remove the large errors of the quadrature Q near the left endpoint, $\alpha_j = 0$. A similar correction can be found near the right endpoint, $\alpha_j = \pi$. The globally uniform $O(h^5)$ approximation is

$$\int_0^\pi G \, d\alpha \approx Q[G] + w_1(\alpha_j) E[B^{le}]^h_{[0,\alpha_j L]} + w_2(\alpha_j) E[B^{ri}]^h_{[\pi-\alpha_j L,\pi]}, \qquad (3.12)$$

where the weights w_1 and w_2 are positive, add up to one, vanish at one or the other endpoint sufficiently fast, and are smooth and periodic. We choose $w_1 = \sin^4(\alpha_j)/(\sin^4(\alpha_j) + \cos^4(\alpha_j))$ and $w_2 = \cos^4(\alpha_j)/(\sin^4(\alpha_j) + \cos^4(\alpha_j))$. Figures 2 (d, e) plot the error in the initial velocity of the axisymmetric vortex sheet computed with the corrected quadrature rule (3.12). As the figures show, the large errors near the axis have been removed, and the error converges uniformly as $O(h^5)$.

This concludes the description of the corrected uniformly $O(h^5)$ quadrature rule for the axisymmetric case. A final comment relates to the Fourier filtering scheme used. Figure 2(f) plots the magnitude of the Fourier coefficients $\hat{e}_k$ of the complex error $e_u + i e_v$. The high wavenumber modes have significantly smaller magnitude than in Fig. 2(c), and can be shown to decay as $O(h^6)$. However, the high modes of the discretization error have not been eliminated and grow under the Kelvin–Helmholtz instability of the sheet. To prevent the growth of these modes they are removed using Krasny's Fourier filter: All modes in the vortex sheet position below a given filter level τ are set to zero at each timestep. The filter level needs to be at least as large as the size of the high modes in the discretization error in the velocity (Fig. 2f) times the timestep Δt. The computations in the next section are performed with $N = 100, 200, 400$ and $0.0002 \leq \Delta t \leq 0.005$, allowing for filter levels as small as $\tau = 10^{-l}$, with $l = 20$.

Notice that this is a difference between the current method and the one based on mesh refinement described by Nie and Baker [22]. In their method, the error is forced to be uniform across the axis and is thereby smooth, allowing for arbitrarily small filter levels. In the present case, the filter level τ is reduced by simultaneously increasing N. However, this is not a problem since for convergence it is required that $N \to \infty$ and $\tau \to 0$ simultaneously [9]. The accuracy of the current method is expected to be comparable to that of Nie and Baker's [22] method.

Machine precision is chosen so that it lies below the applied filter level. The computations are performed with $l = 14, 17, 20$. The ones with $l = 14$ are performed in double machine precision; the ones with $l = 17, 20$ are performed in quadruple machine precision. The planar computations are performed with the same filter level as the axisymmetric ones.

4. NUMERICAL RESULTS

This section presents the computed results for the planar and axisymmetric vortex sheet evolution. As discussed in the previous section, the planar results were computed with both van de Vooren's method [31] and the alternate point vortex approximation [28]. The axisymmetric results were computed with the corrected quadrature rule (3.12).
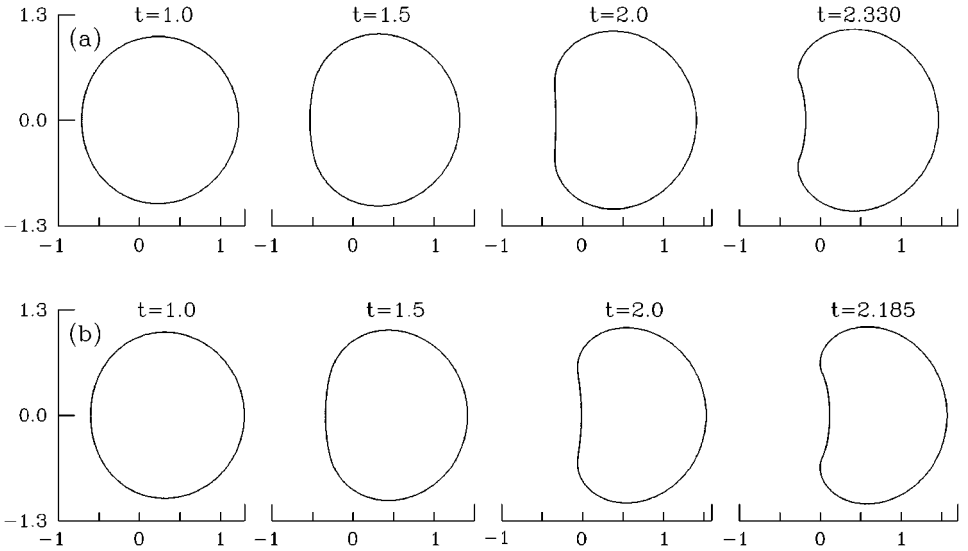
FIG. 3. Computed solution at the indicated times, using $N = 200, l = 14$. (a) Planar. (b) Axisymmetric.

4.1. Evolution of Vortex Sheet and Curvature

Figure 3 plots the computed planar and axisymmetric vortex sheets $(x(\alpha, t), y(\alpha, t))$, $0 \leq \alpha \leq \pi$, at the indicated times, using $N = 200$ and filter level $\tau = 10^{-l}$ with $l = 14$. For clarity, the symmetric image corresponding to $-\pi \leq \alpha \leq 0$ is also plotted. Each sheet moves in the direction of the given impulse and changes shape. The front vorticity causes vortex elements in the rear to decrease in radius, while the rear vorticity causes vortex elements in the front to increase in radius. Since elements with smaller radii travel faster, the rear elements move towards the front ones and the shape of the vortex sheets becomes narrower. The self-induced velocities are larger in the axisymmetric case: The rear approaches the front faster, causing the axisymmetric sheet to become narrower than the planar one.

The vortex sheet curvature in the $x-y$ plane is defined as

$$\kappa(\alpha, t) = \frac{x_\alpha y_{\alpha\alpha} - x_{\alpha\alpha} y_\alpha}{\left(x_\alpha^2 + y_\alpha^2\right)^{3/2}}. \tag{4.1}$$

Initially, $\kappa(\alpha, 0) = 1$ for all α. As the sheet becomes narrower and the rear travels towards the front, the curvature in the rear decreases and becomes negative shortly before $t = 2$, while it remains positive over the remainder of the sheet. At the point where the curvature changes sign it soon blows up in magnitude. The maximal curvature increases to values bigger than 1000 in a timeframe which is only a fraction of the total time evolution, giving a strong indication of the formation of a finite time singularity. This is illustrated in Fig. 4(a), which plots the inverse of the maximal curvature κ_{max} as a function of time. In both the planar and the axisymmetric cases, the inverse maximal curvature decreases slowly until approximately $t = 2.30$ (planar) and $t = 2.16$ (axisymmetric), when it suddenly decreases rapidly and appears to approach zero in finite time. The transition from slow to rapid decrease is sharper in the axisymmetric case. The cause for such a sharp transition region remains unexplained.
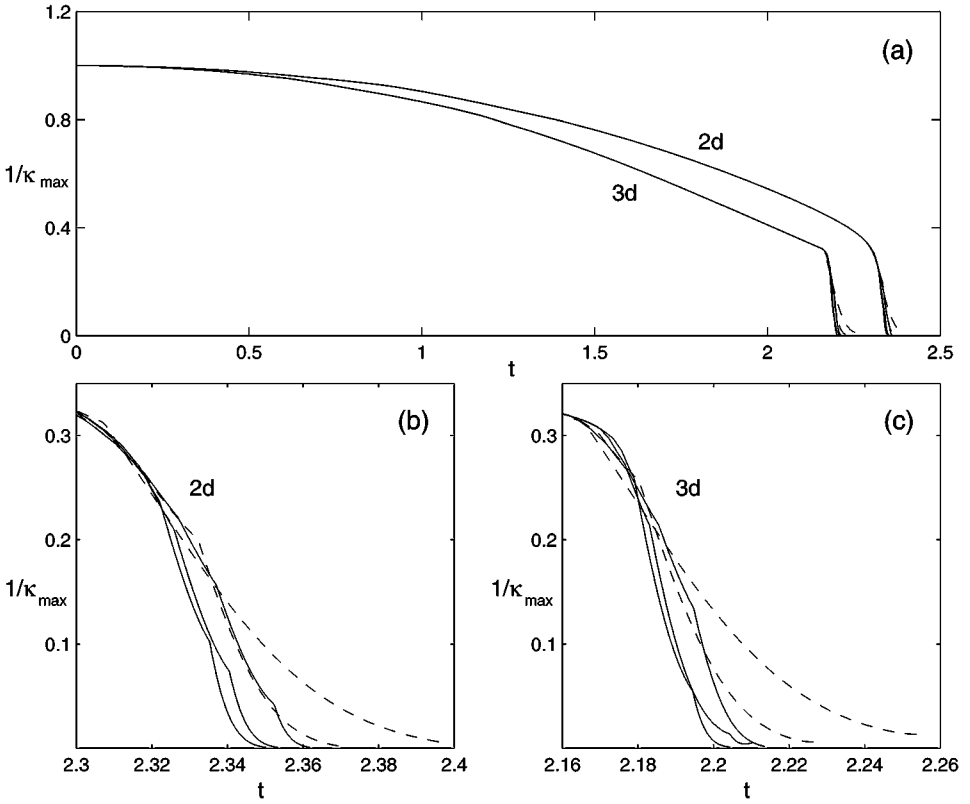
FIG. 4. Evolution of $1/\kappa_{max}(t)$, where κ_{max} is the maximal curvature at time t. Parts (b,c) are close-ups of Part (a). The solid lines are computed with fixed $N = 400$ and varying $l = 14, 17, 20$; the dashed lines are computed with fixed $l = 14$ and varying $N = 100, 200$. Both N and l increase from right to left.

Figures 4(b, c) are close-ups of Fig. 4(a). The solid curves shown are computed with fixed $N = 400$ and varying $l = 14, 17, 20$. The dashed curves are computed with fixed $l = 14$ and varying $N = 100, 200$. Both N and l increase from right to left, with the most resolved result furthest to the left. The kinks in the curves are an artifact of the discretization caused by the fact that the singularity does not occur at a grid point. The figures show that near the apparent singularity formation, the computed solution has not converged in the parameters N and l, and that both parameters need to be increased to better resolve the singularity and gain information about it. For example, the critical time of singularity formation, given by the time when the inverse maximal curvature becomes zero, can only be determined to two significant digits from the data in Fig. 4. The next section presents an alternative approach used to obtain more precise information about the singularity.

4.2. Evolution of Fourier Spectrum

Following previous work, the singularity formation is studied through the analytic continuation of $z(\alpha, t) = x(\alpha, t) + i y(\alpha, t)$ into the complex ξ-plane, where $\xi = \alpha + i\beta$. The idea is to show that $z(\xi, t)$ has a singularity at a point ξ_o in the complex plane, of the form

$$C(t)(\xi - \xi_o(t))^{\mu(t)}, \tag{4.2}$$

where $\xi_o(t) = \alpha_c(t) + i\eta(t)$ and $\mu(t) = p(t) + i\nu(t)$. If $\xi_o(t)$ hits the real axis in finite time, that is, $n(t) \to 0$ as $t \to t_c$, then this establishes the formation of a branch point singularity of order $p(t_c)$ in the vortex sheet. The values of $C(t), \xi_o(t)$, and $\mu(t)$ are typically determined from the asymptotic behaviour of the Fourier coefficients of $z(\xi, t)$ [2, 8, 17, 22, 25–28, 30].

In the present case, $z(\alpha, t) = \overline{z(-\alpha, t)}$ due to the symmetry of the vortex sheets, where the overline denotes the complex conjugate and the sheets are extended to $[-\pi, \pi]$ by symmetry. This implies that $z(\xi, t) = \overline{z(-\bar{\xi}, t)}$, and that if z has a singularity at ξ_o of the form (4.2), it also has a symmetric singularity at $-\bar{\xi}_o$ of the form

$$\bar{C}(t)e^{-i\pi\bar{\mu}}(\xi + \bar{\xi}_o(t))^{\bar{\mu}(t)}. \tag{4.3}$$

The singularities at ξ_o and $-\bar{\xi}_o$ lie both either in the lower complex ξ-plane, or in the upper complex ξ-plane. The asymptotic behaviour of the Fourier coefficients

$$c_k = \frac{1}{2N} \sum_{j=-N+1}^{N} z(\alpha_j, t)e^{-ik\alpha_j} \tag{4.4}$$

follows from results in Carrier *et al.* [10], (section, 6.2) and is given by

$$c_k \approx \frac{A}{k^{p+1}} e^{-\eta k} \sin(k\alpha_c + \nu \ln k + \phi), \tag{4.5a}$$

$$c_{-k} \approx \frac{A}{k^{p+1}} e^{-\eta k} \sin(k\alpha_c + \nu \ln k + \phi) \tag{4.5b}$$

as $k \to \infty$. Equation (4.5a) is satisfied if there are two singularities in the lower half plane, at $\pm\alpha_c - i\eta, \eta > 0$. Equation (4.5b) is satisfied if there are two singularities in the upper half plane, at $\pm\alpha_c + i\eta$. If (4.5) holds, the coefficients oscillate, with an envelope that decays exponentially if $\eta > 0$ and algebraically if $\eta = 0$. Pugh [25] investigated both the behaviour of c_k and c_{-k} to demonstrate singularity formation in a planar Boussinesq bubble by showing that $\eta(t) \to 0$ as $t \to t_c$. Rottman and Stansby [27] used a similar approach for the initially cylindrical vortex sheet studied here and obtained an estimate for the critical time. Nie and Baker [22] investigated the behaviour of the Fourier coefficients for the initially spherical vortex sheet. This section compares the planar and axisymmetric vortex sheet evolution by comparing the behaviour of the respective Fourier coefficients.

Figure 5 plots the absolute coefficients $|c_k|$ at a sequence of increasing times, computed with $N = 400, l = 20$, for the planar and axisymmetric case. The coefficients oscillate and the upper envelope of the oscillations becomes closer to linear as time increases, indicating the transition from exponential to algebraic decay and therefore that $\eta \to 0$ in finite time. The reference line drawn in the figure has slope -2.5, which corresponds to a branch point singularity with $p = 3/2$ and $\eta = 0$. It is, however, difficult to deduce the precise values of $p(t_c)$ and t_c from this figure.

To obtain more precise information, we follow previous work [2, 8, 22, 25, 26, 28] and determine the six parameters $A, p, \eta, \alpha_c, \nu, \phi$ that satisfy (4.5) for consecutive coefficients $c_{k-2}, \ldots, c_{k+3}$, for a range of values of k. For each value of k, the resulting nonlinear system is solved using netlib's iterative solver *dsos* [21]. The initial iterate is either the result for the previous value of k, or it is obtained by the following procedure. Set $p + 1 = 0$ and use a linear least squares fit of the local maxima of c_k to obtain η and $\ln(A)$, and set $\nu = 0$
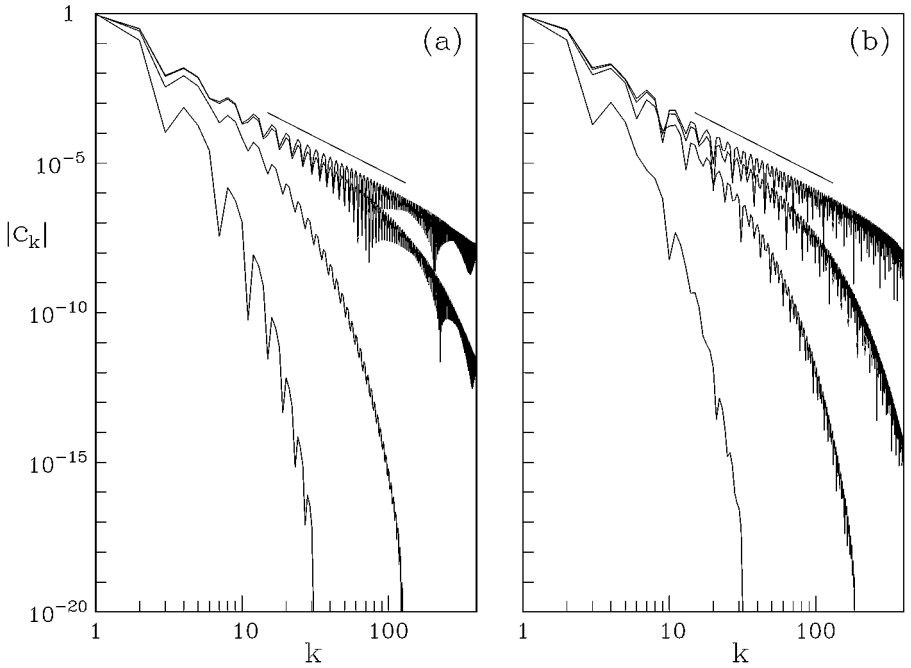
FIG. 5. Fourier coefficients $|c_k|$ vs. k, computed with $N = 400$, $l = 20$. (a) Planar, $t = 1, 2, 2.3, 2.33$. (b) Axisymmetric, $t = 1, 2, 2.14, 2.185$. The coefficients increase with increasing time.

and use a linear least squares fit of the zeroes of the oscillation to obtain ϕ and α_c. This initialization was necessary for the first value of k used, as well as in a few cases when the initialization based on the previous value of k did not lead to converged results. Remaining outliers were removed by a three-point median filter. The values for A, p, η, α_c, ν, ϕ obtained in this way are functions of k. We are interested in the asymptotic regime in which (4.5) holds and these functions are close to constant.

Following Pugh [25] we investigate the behaviour of the coefficients c_k and c_{-k} of the function $z(\alpha, t)$. As mentioned earlier, c_k and c_{-k} give information about singularities in the lower and upper half of the complex ξ-plane, respectively. We will see below that the coefficients c_k that we can resolve are far from the asymptotic regime in which (4.5) holds and do not give precise information about the corresponding singularities. However, we observed that if one shifts the index and considers $\tilde{c}_k = c_{k+2}$, these shifted coefficients approach their asymptotic regime faster. Notice that

$$\tilde{c}_k = \frac{1}{2N} \sum_{J=-N+1}^{N} e^{-2i\alpha_j} z(\alpha_j, t) e^{-ik\alpha_j}, \tag{4.6}$$

and therefore $\tilde{c}_k$ are the Fourier coefficients of $\tilde{z}(\alpha, t) = e^{-2i\alpha} z(\alpha, t)$. Since $\tilde{z}(\alpha, t)$ has the same singularities as $z(\alpha, t)$, the behaviour of $\tilde{c}_k$ gives information about the singularities of z.

Figures 6 (planar) and 7 (axisymmetric) plot the parameters η, p, and α_c obtained for c_k, c_{-k}, and $\tilde{c}_k$ at a sequence of increasing times (see caption), for two different resolutions, $N = 200$, $l = 17$ (dashed lines) and $N = 400$, $l = 20$ (solid lines). The remaining parameters
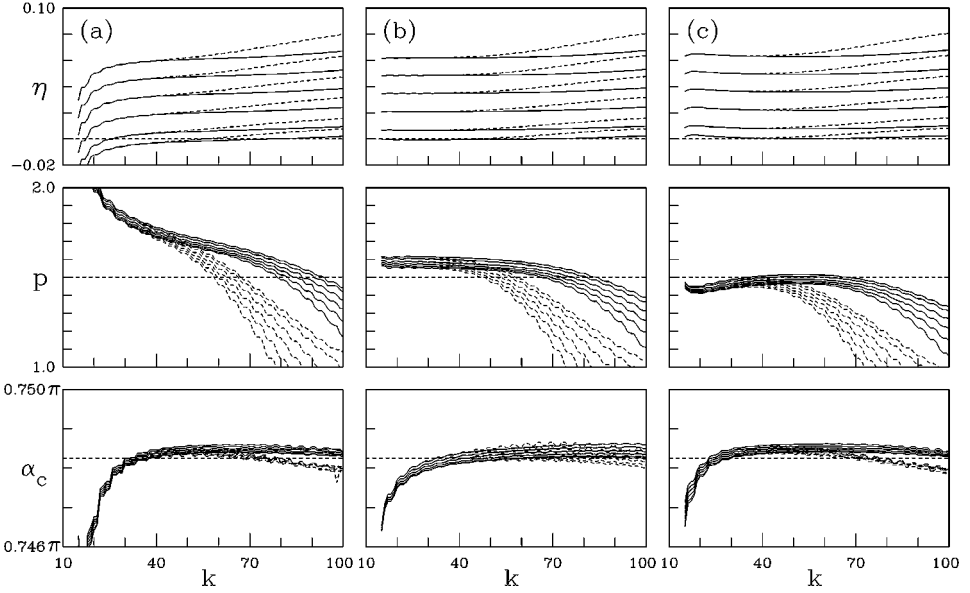
FIG. 6. Planar case. Parameters η, p, α_c in approximation (4.5) obtained from (a) c_k, (b) c_{-k}, and (c) c'_k, computed with $N = 200$, $l = 17$ (dashed) and $N = 400$, $l = 20$ (solid). The data are shown at $t = 2.24, 2.26, 2.28, 2.30, 2.32, 2.33$. The values of η, α_c decrease and the values of p increase with increasing time.
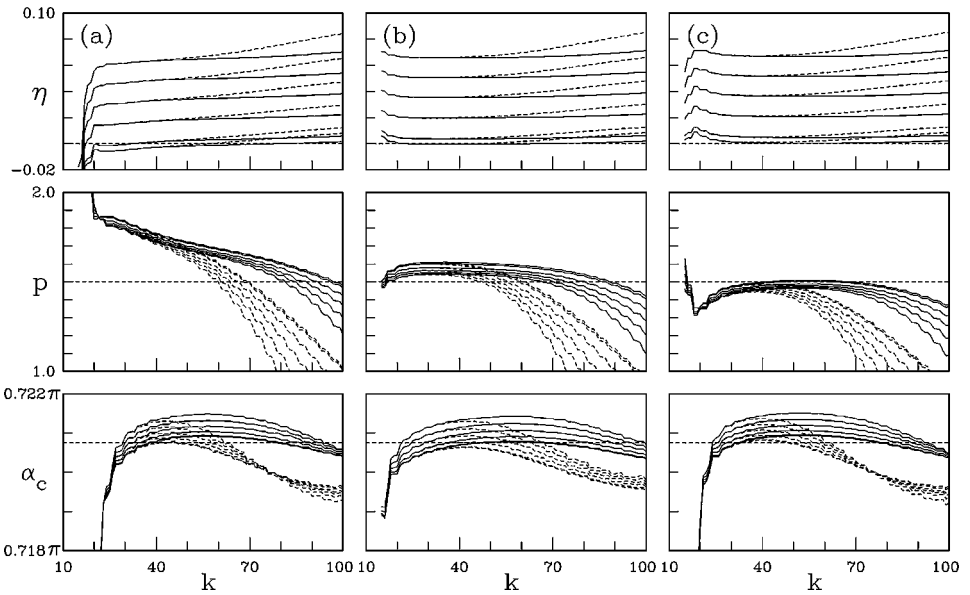

FIG. 7. Axisymmetric case. Parameters η, p, α_c in approximation (4.5) obtained from (a) c_k, (b) c_{-k}, and (c) c'_k, computed with $N = 200$, $l = 17$ (dashed) and $N = 400$, $l = 20$ (solid). The data are shown at $t = 2.10, 2.12, 2.14, 2.16, 2.18, 2.185$. The values of η, α_c decrease and the values of p increase with increasing time.

A, ν, and ϕ are not shown, since not much information is gained from them. The values of p in the figure increase in time, while the values of η and α_c decrease in time. We first discuss the results for c_k in column (a) of Figs. 6 and 7 and then address the results for c_{-k} and $\tilde{c}_k$ in columns (b) and (c).

Consider the results for c_k in Figs. 6(a) and 7(a). The values for η, p, and α_c appear to have converged in N and l for $k \leq 40$ and we focus on these converged values. The values indicate the presence of a singularity in the lower complex ξ-plane which appears to hit the real axis since η appears to approach zero. Note that the planar and axisymmetric values for η, p are almost identical. Both η and p are, however, far from being constant in k, indicating that k is not in the asymptotic regime in which (4.5) holds. Thus, a singularity appears to occur in both the planar and the axisymmetric case, but the precise value of p or t_c cannot be determined from these results. On the other hand, the values of α_c that give the position of the singularity can be determined quite accurately since they are almost constant in k. For $k \geq 25$, $\alpha_{c,2d} \approx 0.748\pi$ with variations of less than 0.1%, and $\alpha_{c,3d} \approx 0.721\pi$ with variations of less than 2%.

The value of $\alpha_{c,3d}$ is slightly smaller than $\alpha_{c,2d}$. This is related to differences in the appearance of the planar and axisymmetric spectra plotted in Fig. 5. Notice that the oscillations of $|c_k|$ in Fig. 5(a) appear more regular than the ones in Fig. 5(b). The oscillations are sampled at $k\alpha_c$ plus a phaseshift. In the planar case, $\alpha_c \approx 0.75\pi$, which means that $(k\alpha_c) \bmod \pi$ repeats itself after every fourth point. Thus every fourth point lies at the same phase in the oscillations, giving much regularity to the plot. In the axisymmetric case $\alpha_c \approx 0.72\pi$. It takes a much larger value of k for $(k\alpha_c) \bmod \pi$ to approximately repeat itself, and this accounts for the apparent irregularity in the plot.

The results in Figs. 6(a) and 7(a) are similar to the results reported by Pugh [25] for the planar Boussinesq bubble and by Nie and Baker [22] for the initially spherical vortex sheet. More precise information about the singularity could be obtained by including higher order terms in the asymptotic behaviour (4.5) of c_k. Shelley [28] implemented such a higher order approximation for a periodically perturbed flat vortex sheet. In that problem, the Fourier coefficients are monotonically decreasing in k and not oscillatory. As a result, six parameters determine the asymptotic behaviour of the coefficients to higher order than in the present case. Instead of introducing even more parameters here, we choose to gain more information by investigating the behaviour of c_{-k} and c'_k.

Figures 6(b, c) and 7(b, c) plot the parameters η, p, α_c obtained for c_{-k} and $\tilde{c}_k$. Based on our comments above, these values relate to singularities of $z(\xi, t)$ in the upper and lower complex ξ-plane, respectively. Surprisingly, these values are much closer to being constant in k than the values for c_k in Figs. 6(a) and 7(a). Thus, c_{-k} and $\tilde{c}_k$ appear to exhibit the asymptotic behaviour (4.5) more closely, and provide more reliable information about the singularity. The reason for this remains unclear. Notice again that the axisymmetric results in Fig. 7(b,c) are almost identical to the planar ones in Fig. 6(b,c). We now use the results obtained from c_{-k} and $\tilde{c}_k$ to gain information about the singularity.

To determine the critical time of singularity formation, Fig. 8 plots the value of η at $k = 40$ for a sequence of times, using the results for c_{-k} (circles) and $\tilde{c}_k$ (crosses). The value at $k = 40$ was taken to be representative of the range in which η has converged and is constant in k. The figure shows that η decreases and reaches zero at the same time, whether it is obtained from c_{-k} or from $\tilde{c}_k$. Thus $z(\xi, t)$ contains singularities in both the upper and the lower complex ξ-plane that hit the real axis at the same critical time. This time, t_c, is
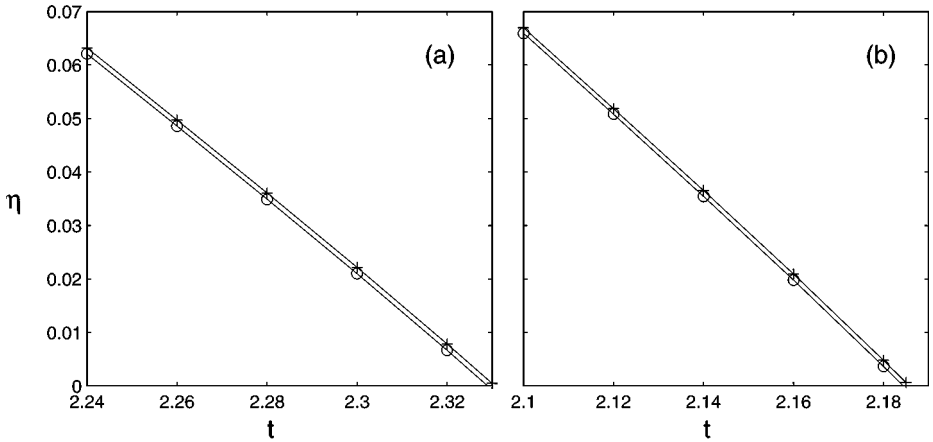
FIG. 8.   Value of η at $k = 40$, vs. time, using the results from Figs. 6(b, c) and 7(b, c). (a) Planar. (b) Axisymmetric.

closely approximated by

$$t_{c,2d} = 2.330, \quad t_{c,3d} = 2.185. \tag{4.7}$$

The planar estimate is lower than the value of $t_c = 2.36$ given by Rottman and Stansby [27]. This is attributed to the fact that they did not investigate convergence in l and used nonuniform values of η obtained from c_k. There are no previous estimates for the axisymmetric critical time.

Notice that the values of $\eta(t)$ in Fig. 8 are almost linear in both the planar and axisymmetric cases. The slope in the planar case is approximately 0.70, while the axisymmetric slope is approximately 0.78. Thus, the axisymmetric singularity approaches the real axis slightly faster.

The values of p in Figs. 6(b) and 7(b), corresponding to a singularity in the upper half plane, increase from 1.5 towards 1.6 as t increases. At any fixed time, however, the values decrease slightly in k, and are consistent with an asymptotic value of $3/2$. The values of p in Figs. 6(c) and 7(c), corresponding to a singularity in the lower half plane, increase from 1.4 to 1.5 as t increases, and are also consistent with an asymptotic value of $3/2$.

Based on the results presented in Figs. 6 and 7, we conclude that in both the planar and axisymmetric case, $z(\xi, t)$ has singularities that hit the axis at a critical time t_c. The formation time t_c and the singularity position $\xi = \alpha_c$ are clearly determined by the Fourier spectrum. The singularity type is consistent with Moore's branch point singularity of order $3/2$ but cannot be pinpointed more precisely since the high wavenumber modes in the asymptotic regime are not well resolved. We can, however, conclude based on the similarity of the two figures that the planar and axisymmetric singularity appear to be of the same type.

One would like to know whether a moderate increase in N and l is sufficient to more precisely identify the singularity type. Figure 9 plots η and p in the planar case for a higher resolution run using $N = 800$, $l = 25$, and quadruple machine precision. The axisymmetric simulation with these parameters was not performed since it requires too much computing time. Figure 9 shows an improvement over the results in Fig 6. The values of
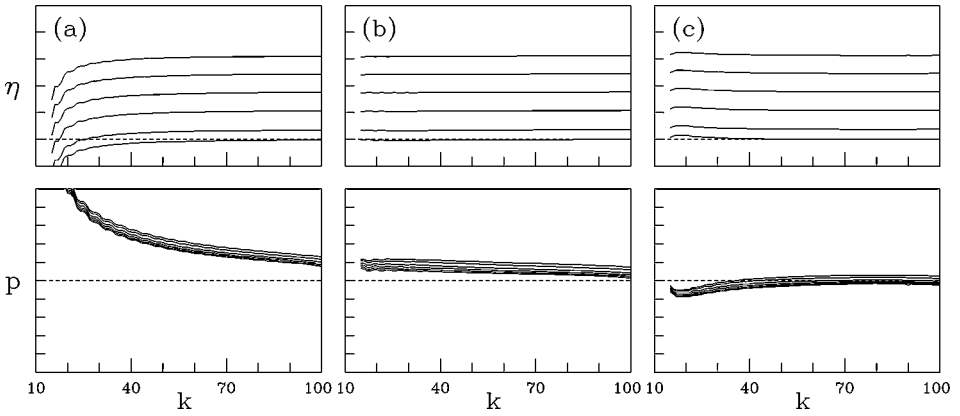
FIG. 9. Planar case. Parameters η, p in approximation (4.5) for (a) c_k, (b) c_{-k}, and (c) c'_k, computed with $N = 400$, $l = 25$. The data one shown for $t = 2.24, 2.26, 2.28, 2.30, 2.32, 2.33$.

η appear to have reached their asymptotic regime, and they confirm the singularity formation time $t_{c,2d} = 2.330$ found previously. The values of p, however, particularly the ones in column (a), remain far from their asymptotic regime. We infer that to more precisely determine the order p of the singularity using the asymptotic expression (4.5) it is necessary to resolve many more Fourier modes. This requires larger values of N and l, which in turn requires arithmetic precision much greater than quadruple machine precision. Further evidence for this is given in the next section. An example of such high accuracy computations is given by Caflisch, Ercolani, and Steele [8] who studied singularities in the steady Boussinesq equations using a multiprecision package with 128 and 200 digits of precision.

4.3. Solution at $t = t_c$

The results in the previous section were used to establish the critical time $t = t_c$ of singularity formation. Figure 10 plots the vortex sheet strength at that time, $\sigma(\alpha, t_c)$, computed with $N = 400$ and $l = 14, 17, 20$. The planar data are shown on the left, the axisymmetric data on the right. The bottom figures show a close-up of the top figures near $\alpha = \alpha_c$. At $t = 0$, the sheet strength is $\sigma(\alpha, 0) = \cos(\alpha)$. The figure shows that in time, $\sigma(\alpha, t)$ has developed a cusp at $\alpha = \alpha_c$. The sheet strength increases as l increases, but the relative variations of the cusp with l are small. The planar and axisymmetric cusp in the close-ups are similar.

Figure 11 plots the curvature at the critical time, $\kappa(\alpha, t_c)$, computed with the same values of N and l as in Fig. 10. The curvature is positive for $\alpha < \alpha_c$, negative for $\alpha > \alpha_c$, and is large at $\alpha = \alpha_c$. The maximum curvature increases somewhat as l is increased. The planar and axisymmetric curvature in Fig. 11(a,b) have noticeable differences away from α_c, but the behaviour near α_c shown in the close-up is quite similar. Notice that small oscillations are visible for the largest value of l shown in the close-up. These oscillations occur when the number of points N is not large enough to resolve the curvature. They represent a type of Gibbs phenomenon that occurs when a high order scheme is used to resolve near singular behaviour. These small oscillations, especially the ones to the right of α_c, are the same in the planar and the axisymmetric case, even though one method is formally exponentially
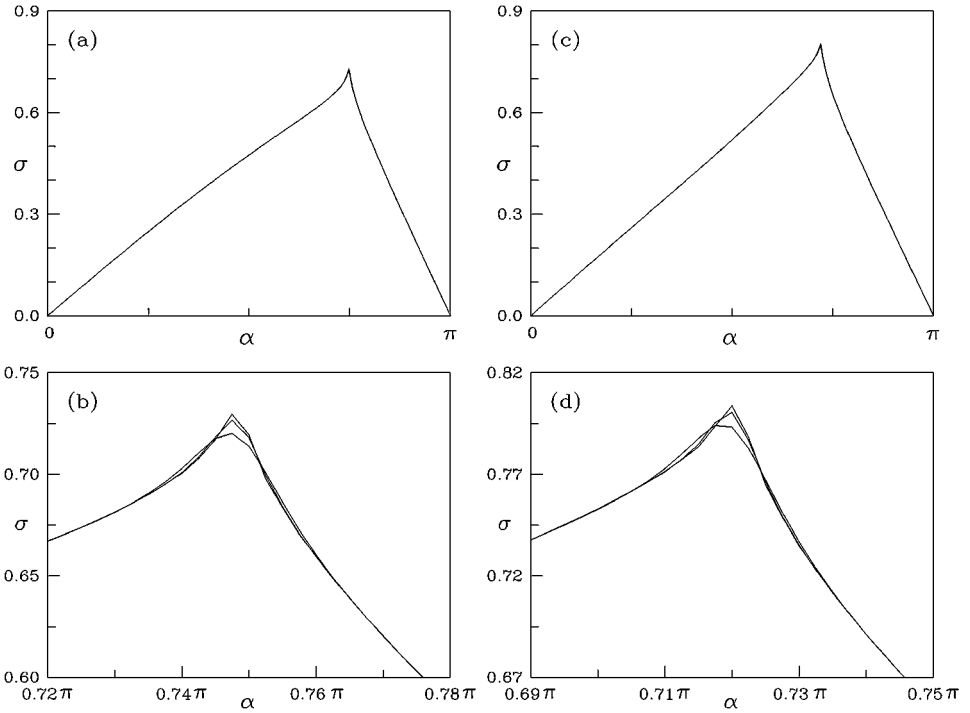
FIG. 10. Vortex sheet strength $\sigma(\alpha, t_c)$ at the critical time, computed with $N = 400$ and $l = 14, 17, 20$. (a,b) Planar. (c,d) Axisymmetric. The bottom figure are close-ups of the top ones near the singularity. The maximum sheet strength increases as l increases.

accurate while the other one is formally $O(h^5)$. We conclude that at the current resolution, there is no visible difference between the exponentially accurate method and the fifth order method. Both methods lose accuracy near the singularity.

Figure 11 clearly shows that the solution at $t = t_c$ is far from being resolved. In the previous section it was claimed that at $t = t_c$, a singularity occurs at which the curvature becomes unbounded, yet in Fig. 11 the maximum curvature is only around 7. The same conclusion can be drawn from Fig. 4. In that figure, the maximal curvature appears to become unbounded in time, but it certainly does not appear to become unbounded at $t = t_c$.

In order to better determine the dependence of the data on the parameters N and l, Fig. 12 plots the maximum vortex sheet strength and the maximum curvature at $t = t_c$, for various values of $N = 200, 400, 800$ and $l = 14, 17, 20, 25$. Both the planar case (—+—) and the axisymmetric one (- -o- -) are shown. The computations with $l = 20$ and $l = 25$ are only computed with $N \geq 400$ and $N \geq 800$, respectively, in order to avoid the oscillations whose beginning could be seen in Fig. 11(c,d). The axisymmetric case is not computed for $N = 800$ and $l \geq 17$, for which quadruple precision is required.

The maximum vortex sheet strength $\sigma_{max}(t_c)$, shown in Fig. 12(a), changes very little as N and l are varied, indicating that it has almost converged, and that the limit as $N, l \to \infty$ is a finite cusp as seen in Fig. 10. This is consistent with a branch point singularity of order $3/2$. On the other hand, the maximum curvature $\kappa_{max}(t_c)$, shown in Fig. 12(b), increases as N and l are increased, indicating that it has not converged and could possibly become unbounded in the limit $N, l \to \infty$. Note that the unboundedness can only be captured if N and l are
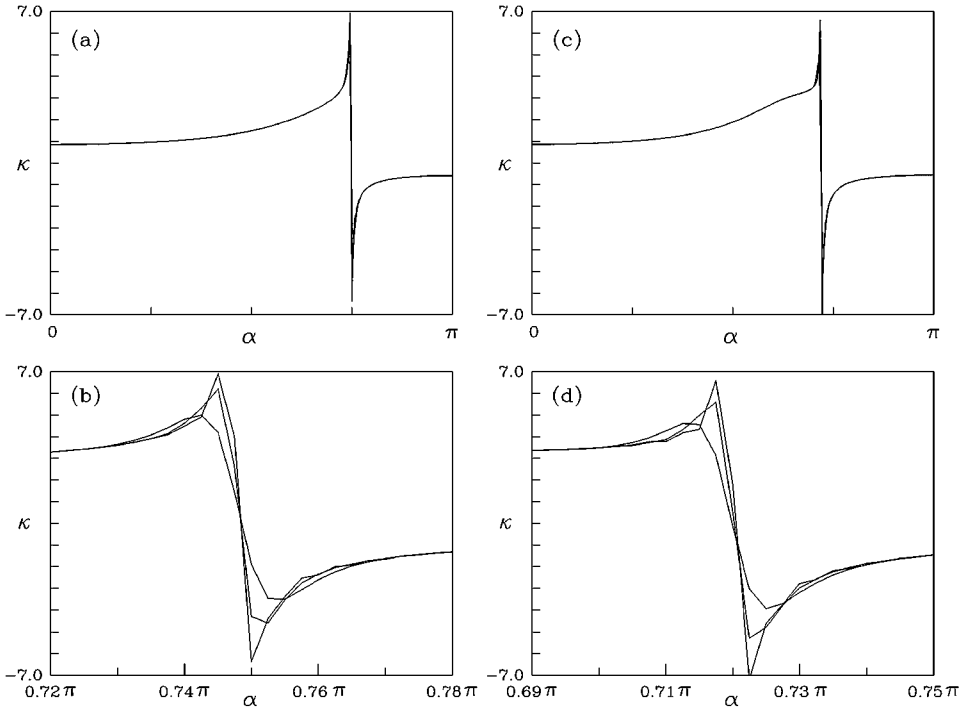
FIG. 11. Curvature $\kappa(\alpha, t_c)$ at the critical time, computed with $N = 400$ and $l = 14, 17, 20$. (a,b) Planar. (c,d) Axisymmetric. The bottom figures are close-ups of the top ones near the singularity. The maximum curvature increases as l increases.
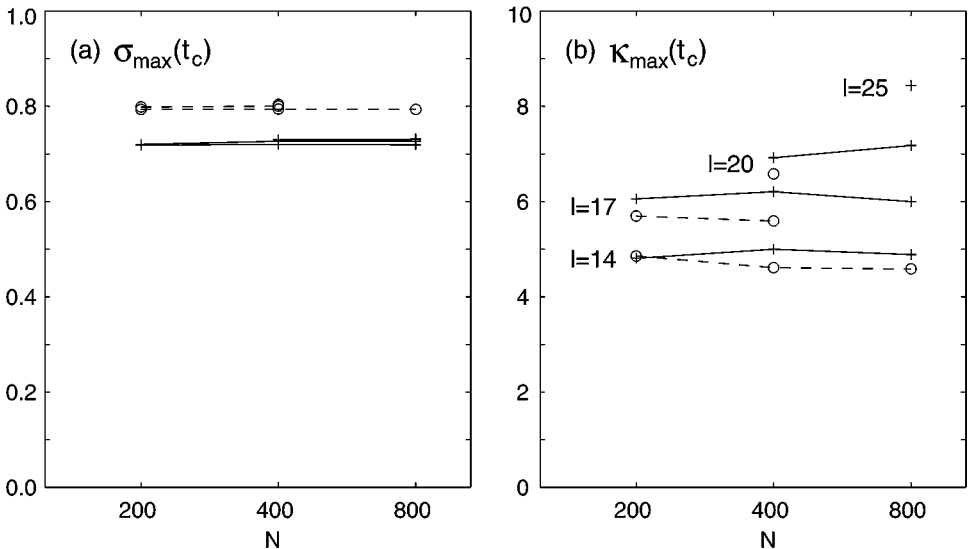

FIG. 12. (a) Maximum vortex sheet strength and (b) maximum curvature at the critical time, for varying values of N and l. Planar case (——, +) and axisymmetric case (– – –, ○). The values of N are indicated on the axis; the values of l increase with increasing values of κ_{max} and σ_{max}, as indicated in Part (b).

increased simultaneously. For fixed filter parameter l, the maximum curvature changes little as $N \to \infty$ and converges towards a finite value. Thus the filter has a smoothing effect, not visible at early times but nonnegligible near the singularity. The effect of the filter has also been addressed by Shelley [28]. For fixed value N, the filter parameter l cannot be increased arbitrarily since otherwise oscillations appear. Thus both N and l have to be increased simultaneously, in agreement with convergence results by Caflisch, Hou, and Lowengrub [9].

Figure 12(b) furthermore shows that the maximum curvature increases slowly in N and l, indicating very low order convergence. Even with $N = 800$ and $l = 25$, the maximum curvature is only around 9. Thus, in order to resolve the singularity and observe the expected blowup in $\kappa_{max}(t_c)$, l needs to be increased significantly, requiring machine precision much below quadruple precision, in agreement with the conclusion at the end of the previous section.

5. SUMMARY

The evolution of an initially cylindrical and an initially spherical vortex sheet were investigated numerically. Based on previous numerical and analytical results it is expected that in the planar case, a branch point singularity of order 3/2 occurs. The goal of the present paper is to gain information about singularity formation in an axisymmetric sheet by comparison with the planar flow. The main results are summarized as follows:

(1) Strong evidence of finite time singularity formation in both the planar and the axisymmetric case is given by (i) the large and sudden increase in the maximal curvature shown in Fig. 4, and (ii) the Fourier spectrum of the evolving sheets, which shows that a singularity in the complex plane hits the real axis in finite time. The singularity formation time t_c and position α_c are accurately determined from the Fourier spectrum.

(2) The planar and axisymmetric singularity type appear to be identical, based on comparison of the Fourier spectrum, the vortex sheet strength and the curvature at the critical time. Some differences between the two flows are observed at a larger scale, for example in the vortex sheet shape and in the curvature away from the singularity.

(3) The computations indicate that the order of the branch point singularity is consistent with 3/2, although it cannot be pinpointed precisely. As is evident from Figs. 4, 10, 11, and 12, the computed solution near the critical time is not well resolved. The results show that to better resolve the flow it is necessary to reduce the filter level significantly, well below quadruple machine precision, and to increase the value of N simultaneously. The difficulty in resolving the flow is independent of whether the flow is planar or axisymmetric.

REFERENCES

1. G. R. Baker, Generalized vortex methods for free-surface flows, in *Waves on Fluid Interfaces*, edited by R. E. Meyer (Academic Press, San Diego, 1983), pp. 53–81.

2. G. Baker, R. E. Caflisch, and M. Siegel, Singularity formation during Rayleigh–Taylor instability, *J. Fluid Mech.* **252**, 51–78 (1993).

3. G. R. Baker, D. I. Meiron, and S. A. Orszag, Boundary integral methods for axisymmetric and three-dimensional Rayleigh–Taylor instability problems, *Physica D* **12**, 19–31 (1984).

4. G. K. Batchelor, *An Introduction to Fluid Mechanics* (Cambridge Univ. Press, Camabridge , UK, 1967).

5. B. de Bernadinis and D. W. Moore, A ring-vortex representation of an axisymmetric vortex sheet, in *Studies of Vortex Dominated Flows*, edited. by M. Y. Hussaini and M. D. Salas (Springer-Verlage, Berlin/New York, 1987), pp. 33–43.

6. M. Brady and D. I. Pullin, On singularity formation in three-dimensional vortex sheet evolution, *Phys. Fluids* **11**, 3198–3200 (1999).

7. R. E. Caflisch, N. Ercolani, T. Y. Hou, and Y. Landis, Multi-valued solutions and branch point singularities for nonlinear hyperbolic or elliptic systems, *Commun. Pure Appl. Math.* **46** (4), 453–499 (1993).

8. R. E. Caflisch, N. Ercolani, and G. Steele, Geometry of singularities for the steady Boussinesq equation, *Selecta Math.* **2**(3), 369–414 (1996).

9. R. E. Caflisch, T. Y. Hou, and J. Lowengrub, Almost optimal convergence of the point vortex method for vortex sheets using numerical filtering, *Math. Comput.* **68**(228), 1465–1496 (1999).

10. G. F. Carrier, M. Krook, and C. E. Pearson, *Functions of a Complex Variable* (McGraw-Hill, New York, 1966).

11. H. D. Ceniceros and H. Si, Computations of axisymmetric suction flow through porous media in the presence of surface tension, *J. Comput. Phys.* **165**(1), 237–260 (2000).

12. S. J. Cowley, G. R. Baker, and S. Tanveer, On the formation of Moore curvature singularities in vortex sheets, *J. Fluid Mech.* **378**, 233–267 (1999).

13. G. Dahlquist and A. Björck, *Numerical Methods* (Prentice-Hall, Englewood Cliffs, N.J., 1974).

14. G. Hu, *Singularity Formation in Three-Dimensional Vortex Sheets*, Ph.D. thesis (California Institute of Technology, 2000).

15. T. Ishihara and Y. Kaneda, Singularity formation in three-dimensional motion of a vortex sheet, *J. Fluid Mech.* **300**, 339–366 (1995).

16. T. Ishihara and Y. Kaneda, Singularity formation in the shape of a vortex sheet in three dimensions—numerical simulation, in *Vortex Flows and Related Numerical Methods II, ESAIM: Proceedings,* Vol. 1, http://www.emath.fr/proc, 1996, pp. 463–479.

17. R. Krasny, 1986. A study of singularity formation in a vortex sheet by the point-vortex approximation, *J. Fluid Mech.* **167**, 65–93 (1986).

18. H. Lamb, *Hydrodynamics*, 6th ed. (Dover, New York, 1932).

19. D. I. Meiron, G. R. Baker, and S. A. Orszag, Analytical structure of vortex sheet dynamics. Part 1. Kelvin–Helmholtz instability, *J. Fluid Mech.* **114**, 283–298 (1982).

20. D. W. Moore, The spontaneous appearance of a singularity in the shape of an evolving vortex sheet, *Proc. R. Soc. London. A* **365**, 105–119 (1979).

21. Netlib routine http://www.netlib.org/slatec/src/dsos.f.

22. Q. Nie and G. Baker, Application of adaptive quadrature to axisymmetric vortex sheet motion, *J. Comput. Phys.* **143**, 49–69 (1998).

23. M. Nitsche, Evolution of a cylindrical and a spherical vortex sheet, in *Vortex Flows and Related Numerical Methods II, ESAIM: Proceédings,* Vol. 1, http://www.emath.fr/proc, 1996, pp. 401–414.

24. M. Nitsche, Axisymmetric vortex sheet motion: accurate evaluation of the principal value integral, *SIAM J. Sci. Comput.* **21**(3), 1066–1084 (1999).

25. D. A. Pugh, Development of Vortex Sheets in Boussinesq Flows—Formation of Singularities, Ph.D. thesis (Imperial College of Science and Technology, 1989).

26. M. C. Pugh and M. J. Shelley, Singularity formation in thin jets with surface tension, *Commun. Pure Appl. Math.* **51**(7), 733–795 (1998).

27. J. W. Rottman and P. K. Stansby, On the δ-equations for vortex sheet evolution, *J. Fluid Mech.* **247**, 527–549 (1993).

28. M. Shelley, A study of singularity formation in vortex-sheet motion by a spectrally accurate vortex method, *J. Fluid Mech.* **244**, 493–526 (1992).

29. A. Sidi and M. Israeli, Quadrature methods for periodic singular and weakly singular Fredholm integral equations, *J. Sci. Comput.* **3**(2), 201–231 (1988).

30. C. Sulem, P.-L. Sulem, and H. Frisch, Tracing complex singularities with spectral methods, *J. Comput. Phys.* **50**, 138–161 (1983).

31. A. I. van de Vooren, A numerical investigation of the rolling up of vortex sheets, *Proc. R. Soc. London A* **373**, 67–91 (1980).